CLIMATOLOGY

Subpolar North Atlantic cooling reinforced by colder, drier atmosphere with a weakening Atlantic meridional overturning circulation

Yifei Fan[1], Duo Chan[2], Eugene E. Clothiaux[1], Pengfei Zhang[1]*, Laifang Li[1,3,4]

In contrast to global warming, the subpolar North Atlantic has experienced long-term cooling throughout the 20th century. This cooling, known as the North Atlantic cold blob, has been hypothesized to arise from reduced poleward oceanic heat transport associated with a slowdown of the Atlantic meridional overturning circulation (AMOC). Here, by diagnosing historical simulations from multiple coupled climate models, we find that ocean heat transport is not the only pathway through which the AMOC modulates sea surface temperature variability. A weakened AMOC is also associated with colder, drier lower atmospheric conditions, which lead to a reduction in surface warming expected from increasing amounts of heat-trapping gases by reducing downward clear-sky longwave radiation at the surface. This radiative pathway and the oceanic processes contribute equally to the North Atlantic cold blob. These results highlight the importance of the AMOC's impact on atmospheric properties and their radiative effects.

INTRODUCTION

In contrast to global warming since industrialization (*1*), sea-surface temperature (SST) over the subpolar North Atlantic (25°W-45°W, 50°N-60°N) has cooled at a rate of 0.15 (±0.12; SD) K/century from 1900 to 2014 (Fig. 1A and fig. S1). This cooling, known as the North Atlantic "cold blob" (*2*, *3*) or "warming hole" (*4*–*7*), signifies a distinct role of the subpolar North Atlantic in absorbing excessive heat from anthropogenic forcing (*8*). By buffering the ocean surface from immediate warming (*9*), the cold blob not only influences local weather and climate, such as jet streams, storm tracks, and European weather, but also has far-reaching effects on the intertropical convergence zone (*10*–*13*), global distribution of marine heat waves, and transient warming (*9*, *14*). This pattern of SST changes also affects marine organisms and fisheries productivity in the North Atlantic (*15*). Thus, understanding the causes of the North Atlantic cold blob has long been desired (*4*, *5*).

To date, a weakening of the Atlantic meridional overturning circulation (AMOC) has been proposed as the main driver of the North Atlantic cold blob (*6*, *7*). Although a lack of direct observations of the AMOC leaves its past variability an open question (*6*, *16*, *17*), extensive evidence from paleo databases and climate modeling experiments supports a relationship between changes in AMOC and North Atlantic SSTs on decadal and longer timescales (*18*–*23*). Substantial AMOC declines in the past, sometimes with a temporary shutdown, have triggered abrupt North Atlantic cooling, including the 8.2 ka event in the early Holocene (*23*) and the Younger Dryas and multiple Heinrich events in the last glacial period (*22*). With continued global warming, the AMOC is projected to weaken substantially by the end of the 21st century (*21*, *24*), resulting in a lack of warming in the North Atlantic (*21*).

The AMOC has been thought to modulate low-frequency SST variability in the North Atlantic by changing poleward heat transport (*25*). A weakened AMOC would lead to reduced heat transport into the subpolar ocean, resulting in a local heat deficit and surface cooling (*26*). However, as the ocean is actively coupled to the atmosphere in the subpolar North Atlantic, SST changes in this region are modulated by various factors through multiple pathways. On decadal and longer timescales, subpolar North Atlantic SST variability is modulated by oceanic heat transport (*27*), air-sea heat fluxes (*28*, *29*), mixed layer entrainment (*30*), and atmospheric radiation (*31*), which are subject to atmospheric variability, such as the North Atlantic Oscillation (*32*). As such, wind-driven gyre circulation changes (*33*), a more positive North Atlantic Oscillation (*3*), jet stream intensification (*34*), and increased storminess (*2*) have also been proposed to explain the formation of the cold blob. Studies suggest that North Atlantic atmospheric circulation is, to some extent, interlinked with AMOC variability (*10*, *32*). Thus, the way the AMOC may induce the cold blob in the past century, whether through ocean heat transport or responses of the atmosphere, remains to be addressed.

This study investigates the role the AMOC plays in North Atlantic cold blob formation within a suite of state-of-the-art climate models and quantifies its influence through an ocean heat budget analysis. Our findings reveal that the AMOC trend explains two-thirds of the simulated cooling trend in the subpolar North Atlantic, with equal contributions from oceanic and radiative processes. As to be demonstrated here, on decadal timescales, AMOC weakening reduces both ocean heat transport convergence (OHTC) and turbulent heat loss from the ocean in the subpolar North Atlantic. These changes are followed by lower troposphere cooling and drying, which decreases downward longwave radiation and further intensifies sea surface cooling. This research advances our understanding of AMOC's role in North Atlantic SST variability by elucidating accompanying atmospheric changes and radiative effects.

RESULTS

We examine historical SSTs simulated by state-of-the-art fully coupled climate models participating in the 6th phase of the Coupled Model

[1]Department of Meteorology and Atmospheric Science, Pennsylvania State University, University Park, PA 16802, USA. [2]School of Ocean and Earth Science, University of Southampton, Southampton, Hampshire, UK. [3]Institute of Computational and Data Sciences, Pennsylvania State University, University Park, PA 16802, USA. [4]Earth and Environmental Systems Institute, Pennsylvania State University, University Park, PA 16802, USA.
*Corresponding author. Email: pfz5053@psu.edu

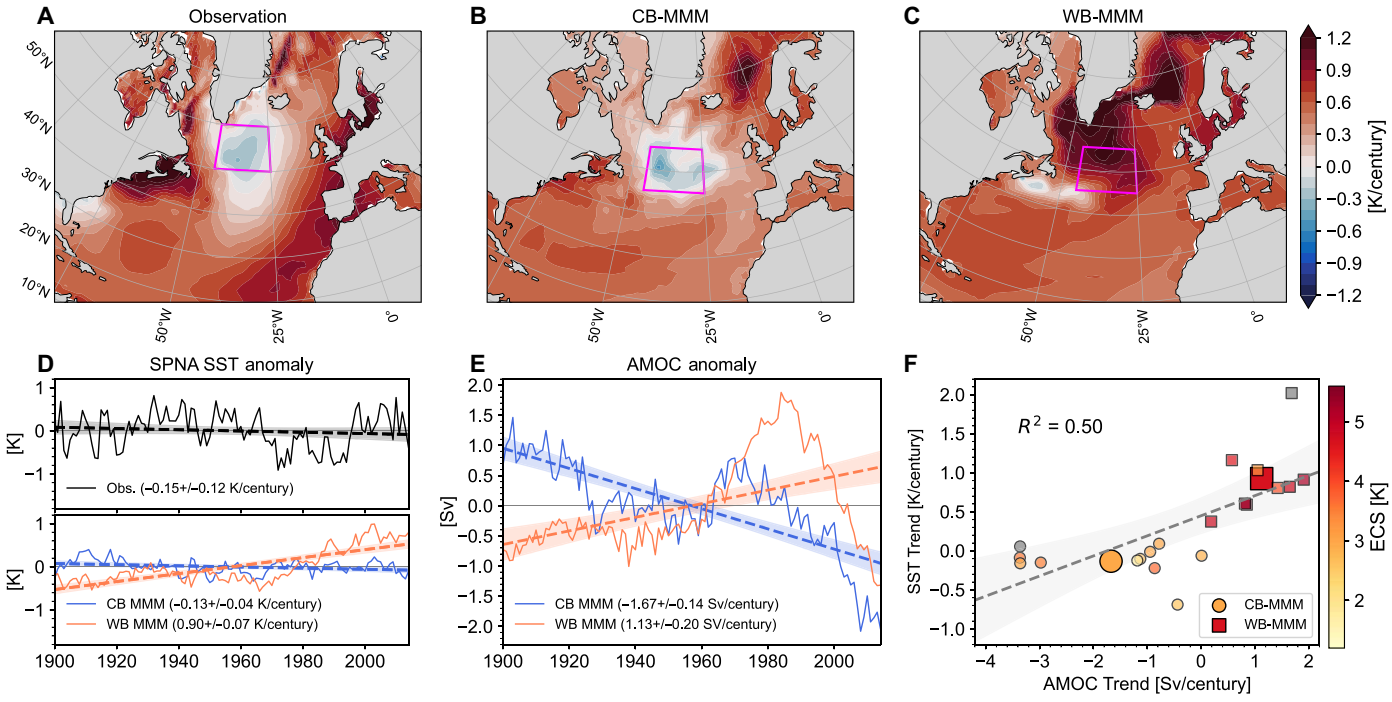

Fig. 1. The Subpolar North Atlantic SST trend, the AMOC trend, and the intermodel relationship between the two. (**A**) Observed linear SST trends from 1900 to 2014, estimated as the average of ERSSTv5, HadISST, and Kaplan SSTs (Materials and Methods). (**B**) Same as (A) but for the multimodel means (MMMs) across the 11 cold blob (CB) models. (**C**) Same as (B) but for the MMMs across the nine warm blob (WB) models. The magenta box in [(A) to (C)] represents the domain of the subpolar North Atlantic. (**D**) Time series of subpolar North Atlantic (SPNA) SST anomalies in the observations (*black*), the CB-MMMs (blue), and the WB-MMMs (red). For observations, the SPNA regional mean is calculated over the domain of 25°W-45°W and 50°N-60°N, as shown by the box in (A); for CB- and WB-MMMs, it is calculated over the domain of 25°W-45°W and 45°N-55°N, as shown by the box in [(B) and (C)]. (**E**) Time series of AMOC index anomalies averaged across the CB models (blue) and the WB models (red). Linear regressions (dashed lines) and corresponding 95% confidence intervals (shading) for the data in [(D) and (E)] are also illustrated. The linear trends and their corresponding SDs are provided in the legends. (F) Simulated subpolar North Atlantic SST trend versus AMOC trend for each model, together with the linear regression (dashed line) across models, associated 95% confidence interval (shading), and explained variance (R^2). Colors indicate model equilibrium climate sensitivity (ECS) values, and models with no available ECS value are marked by gray. The CB and WB models are shown by the small dots and squares, respectively. The CB-MMM and the WB-MMM are indicated by the large dot and square, respectively.

Intercomparison Project (CMIP6) (*35*). The models show a considerable spread in the linear trend of subpolar North Atlantic SSTs from 1900 to 2014 (fig. S2). Of the 32 models, we select 11 that exhibit a long-term cooling in the subpolar North Atlantic for further analysis, referring to them as cold blob models hereafter (see model information in table S1). Conversely, nine models that simulate greater warming in the subpolar basin compared to elsewhere in the North Atlantic are also selected and referred to as "warm blob" models. The cold blob models, on average, reproduce the spatial pattern and magnitude of the observed cold blob, i.e., cooling southeast of Greenland in the central subpolar basin but warming elsewhere in the North Atlantic (Fig. 1, A and B). In the cold blob models, the simulated regional mean SSTs over the subpolar North Atlantic, defined as the region from 25°W to 45°W and from 45°N to 55°N, show an average linear trend of −0.13 (±0.04) K/century, which aligns closely with that observed of −0.15 (±0.12) K/century (Fig. 1D). In contrast, the warm blob models, on average, show substantial warming at a rate of 0.90 (±0.07) K/century in the subpolar North Atlantic (Fig. 1, C and D).

One differentiating factor for the subpolar North Atlantic SST trends in the two model groups is the simulated rate of change in the AMOC (Fig. 1, E and F), defined as the maximum overturning in the stream function in the North Atlantic (Materials and Methods). Overall, differences in the AMOC trends explain 50% of the intermodel spread in the subpolar North Atlantic SST trends ($R^2 = 0.50$; Fig. 1F). Models simulating a greater AMOC decline simulate more cooling over the subpolar North Atlantic, whereas those with an AMOC strengthening trend simulate more warming. Specifically, the cold blob models, on average, simulate an AMOC weakening at a rate of −1.67 (±0.14) Sv/century, whereas the warm blob models show an average AMOC strengthening trend of 1.13 (±0.20) Sv/century (Fig. 1E). This intermodel relationship between the AMOC index and subpolar North Atlantic SST trends aligns with the hypothesized linkage between the weakened AMOC and the cold blob. To identify the physical processes through which the AMOC influences SSTs and quantify their contributions, we apply a partial temperature change decomposition framework (Materials and Methods) to the simulated SSTs in the two groups of models.

Oceanic and radiative processes driving SST trends in the past century

On the basis of the ocean heat budget, the partial temperature change framework (Materials and Methods) decomposes SST trends into seven terms associated with different physical processes: surface albedo feedback (T1); cloud radiative forcing at the surface due to longwave (T2) and shortwave (T3) effects; surface downward clear-sky shortwave irradiance (T4), which is mostly the direct effect of

aerosol forcing; surface downward clear-sky longwave irradiance (T5), which includes effects of atmospheric temperature, water vapor, other greenhouse gases, and/or atmospheric absorbing aerosol; OHTC (T6); and surface latent and sensible heat fluxes (T7). We first evaluate the contributions of the seven physical processes to the simulated long-term SST trends in both the cold blob and warm blob models.

Decreased OHTC in the subpolar North Atlantic provides the greatest contribution to cooling (Fig. 2A, T6), with a resultant SST cooling rate of −2.14 K/century in the subpolar North Atlantic. However, approximately 90% of the OHTC-induced cooling is offset by a decrease in the surface turbulent heat fluxes from the ocean to the atmosphere (Fig. 2A, T7). These changes in the surface turbulent heat fluxes are a spontaneous response of the ocean that minimizes SST anomalies caused by changes in ocean heat transport on multidecadal timescales (*27*, *36*, *37*). The combined effect of changes in the OHTC and surface heat fluxes results in a net cooling rate of −0.15 K/century in the subpolar North Atlantic (Fig. 3A, oceanic). In the warm blob models, the opposite occurs; the OHTC increase leads to a warming trend of 1.36 K/century (Fig. 2B, T6) and the warming is largely counterbalanced by surface heat fluxes (Fig. 2B, T7), resulting in a net warming of 0.21 K/century (Fig. 3B, oceanic). This intergroup difference implies the important contribution of oceanic heat transport to formation of the cold blob (Fig. 3C, oceanic), consistent with previous studies (*26*, *33*).

Notably, atmospheric radiative processes also contribute to the simulated SST trends in the two groups of models (Fig. 2, A and B, T2 to T5). Changes in cloud radiative forcing produce noteworthy SST changes (Fig. 2, A and B, T2 and T3) and show statistically significant intergroup differences (Fig. 2C, T2 and T3). Nevertheless, differences in the longwave and shortwave cloud radiative forcing are similar in pattern and opposite in sign, resulting in cloud-associated intergroup differences in SST trends being negligible. Surface downward clear-sky shortwave radiation decreases as increased amounts of atmospheric aerosol scatter and absorb more solar radiation, resulting in a basin-wide cooling (Fig. 2, A and B, T4), which is present in both the cold blob and warm blob models (Fig. 2C, T4). Last, surface downwelling clear-sky longwave radiation increases due to increased atmospheric temperature, water vapor, other greenhouse gases, and/or atmospheric absorbing aerosols, resulting in basin-wide SST warming (Fig. 2, A and B, T5). However, the resultant warming in the subpolar North Atlantic is minimal in the cold blob models and substantially lower than in the warm blob models (Fig. 2C, T5). This implies the existence of a unique localized radiative process that alleviates clear-sky longwave radiation–induced warming in the cold blob models.

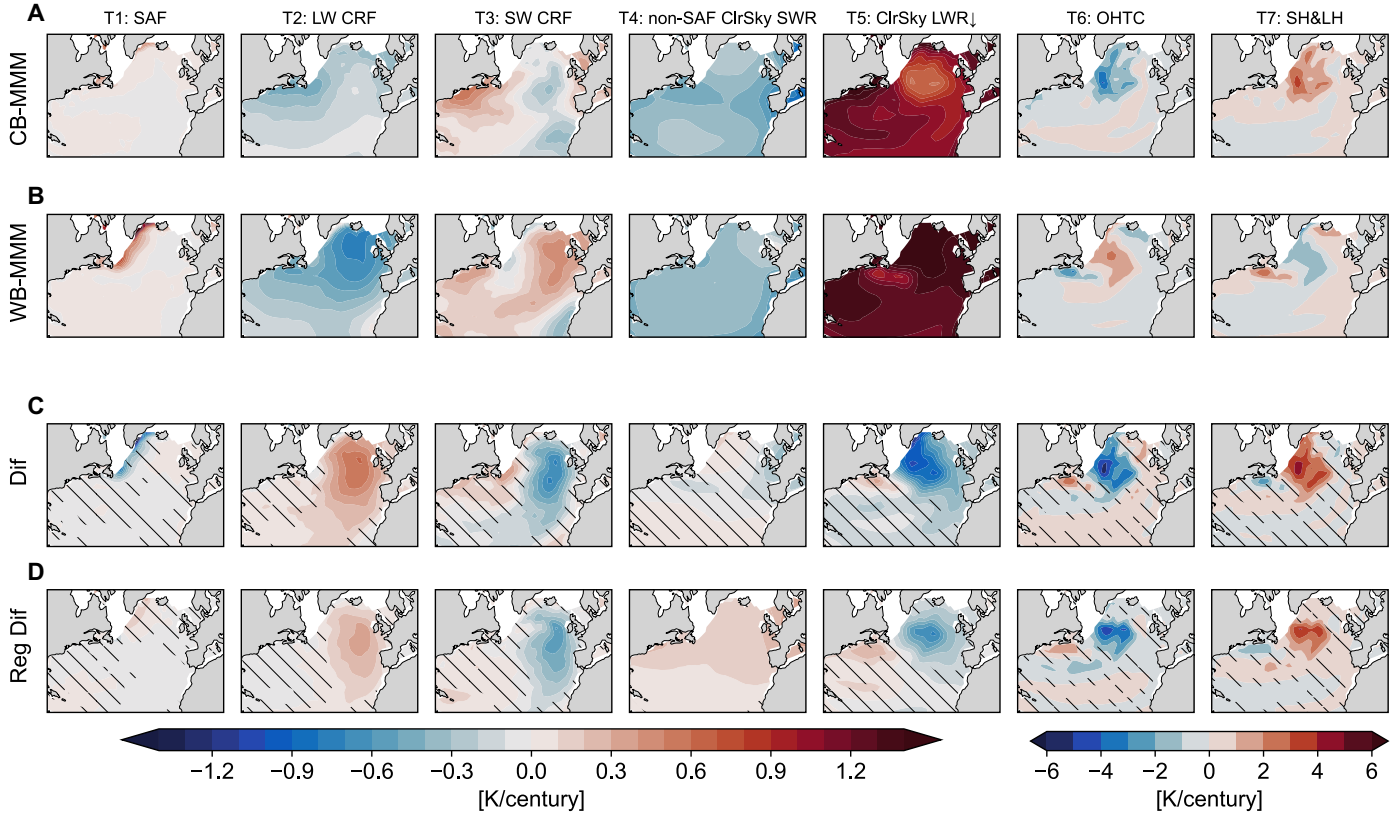

Fig. 2. SST trends induced by the seven different physical processes. The (**A**) CB-MMM and (**B**) WB-MMM SST trends, (**C**) the CB-MMM minus WB-MMM differences in simulated SST trends, and (**D**) the differences in SST trends regressed on the AMOC index trend. From left to right are the seven partial temperature changes due to changes in surface albedo feedback (T1), surface longwave cloud radiative forcing (T2), surface shortwave cloud radiative forcing (T3), surface clear-sky downward shortwave irradiance (T4), surface clear-sky downward longwave irradiance (T5), ocean heat transport convergence (T6), and surface latent heat and sensible heat fluxes (T7). Values in the Labrador Sea and the Nordic Seas are masked because the decomposition error can be non-negligible in these ice-present regions. The hatching in [(C) and (D)] indicates where the CB-MMM minus WB-MMM differences are not statistically significant at the 95% confidence level, estimated via a bootstrapping method.

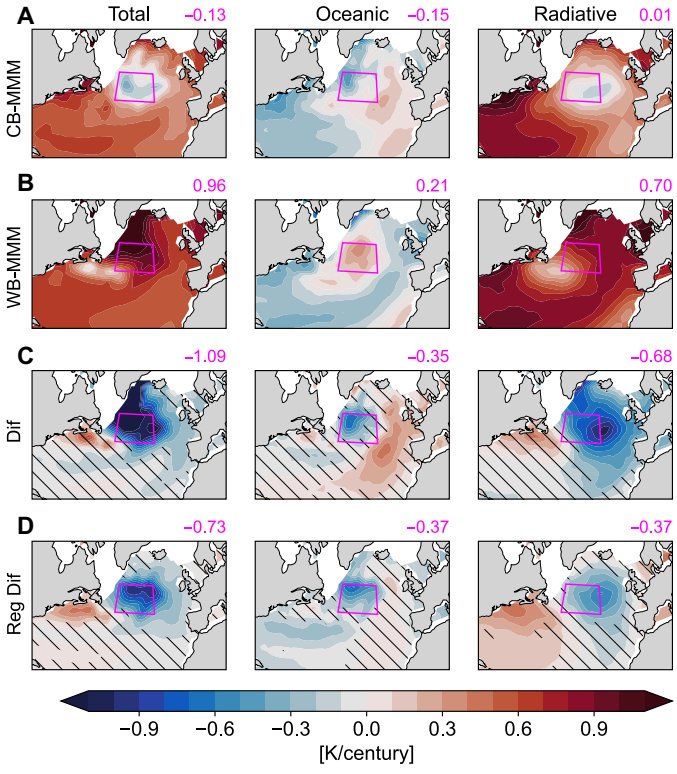

Fig. 3. Total SST trends and SST trends induced by oceanic and radiative processes. (**A**) CB-MMM SST trends, (**B**) WB-MMM SST trends, (**C**) CB-MMM minus WB-MMM differences in SST trends, and (**D**) the differences in SST trends regressed on the AMOC index trend. From left to right are the sum of all terms (total), the sum of T6 and T7 (oceanic), and the sum of T2, T3, T4, and T5 (radiative). The hatching in [(C) and (D)] indicates where the CB-MMM minus WB-MMM differences are not statistically significant at the 95% confidence level. The magenta box in each panel represents the location of the subpolar North Atlantic domain, and the numbers shown at the top right are corresponding domain averages.

Together, changes in cloud radiative effects, clear-sky shortwave radiation, and clear-sky longwave radiation result in a cold blob-like pattern in the cold blob models which is absent in the warm blob models (Fig. 3, A and B, radiative). Among the three terms, clear-sky longwave radiation is the primary differentiator for whether a North Atlantic cold blob is present, as the intergroup difference induced by this process alone exhibits a considerable cooling in the subpolar North Atlantic (Fig. 2C, T5), a pattern similar to the total radiation-induced SST difference (Fig. 3C, radiative). Hereafter, we focus on explaining the differences between the multimodel means of the two model groups. In this way, the homogeneous baseline SST changes in response to external forcings are largely removed and the localized physical processes unique to the formation of the cold blob are highlighted.

Comparison between the contributions of oceanic and radiative processes further demonstrates the importance of localized radiative processes in the formation of the North Atlantic cold blob. Radiative processes not only account for a larger spatial extent but also contribute twice as much as oceanic processes in explaining the intergroup difference in the subpolar North Atlantic SST trends (Fig. 3C, oceanic versus radiative). Oceanic processes are responsible for about one-third (−0.35 K/century) of the total difference in the subpolar North Atlantic domain, whereas radiative processes account for the remaining two-thirds (−0.68 K/century).

Dual impacts of the AMOC on subpolar North Atlantic SSTs

Having evaluated the physical processes responsible for the SST trends, we now assess the role of the AMOC by regressing the partial temperature changes onto the AMOC index (Figs. 2D, 3D, 4, and 5 and figs. S3 and S4). Specifically, we estimate the change in a physical process related to a change in the AMOC as the linear regression coefficient between the detrended, 9-year smoothed physical variable and the AMOC index, with the AMOC index leading by 1 to 3 years (Materials and Methods). The spatial patterns of the regression coefficients for each partial temperature change are, overall, consistent in the subpolar North Atlantic region across the cold blob and warm blob models (Fig. 4, A and C). Therefore, the intergroup differences in the regressed SST trends are primarily due to differences in the AMOC trend, rather than differences in simulated physical processes.

Consistent with the linear intermodel relationship between the AMOC trend and the SST trend (Fig. 1E), the regression analysis suggests that the AMOC is a major contributor to the drastic SST changes in the subpolar North Atlantic region (Figs. 3D, total; and 5, stippled boxes). The simulated AMOC weakening explains the basin-wide cooling in the subpolar North Atlantic and the warming along the Gulf Stream region (Fig. 3D; f4B, top row, total), a pattern closely resembling the previously suggested SST fingerprint of a weakening AMOC (*6*, *19*). Moreover, our analysis shows that AMOC variability imprints not only on OHTC but also on surface downward radiative fluxes (Figs. 2D and 4). In other words, a weakening AMOC may induce a cold blob through two processes at the same time: a direct process via a decrease in OHTC as previously suggested and an indirect response via atmospheric radiative processes. The latter, according to CMIP6 models, is equally important for the formation of the cold blob (Fig. 3D, oceanic versus radiative).

According to our quantification, changes in the AMOC almost completely explain the OHTC-induced SST changes in the central subpolar North Atlantic (Figs. 2D and 5A, T6). Note that the regressed SST change might implicitly include effects from covarying gyre circulation changes due to the inherent coupling between the AMOC and wind-driven circulations (*38*). As discussed above, OHTC-induced SST changes are largely compensated by surface turbulent heat fluxes (Figs. 2D and 5A, T7) via thermal damping (*39*). Therefore, AMOC-associated oceanic processes in total explain an SST trend difference of −0.33 K/century, which is 46% of the total AMOC-associated difference (−0.71 K/century) in the subpolar North Atlantic domain (Figs. 3D, oceanic; and 5B, stippled blue box).

The remaining 54% of the AMOC's fingerprint involves atmospheric radiative processes, primarily clear-sky downward longwave radiation at the surface (Figs. 2D; 5A, T5; and 5B, stippled pink box). Specifically, in the cold blob models, a weakened AMOC is associated with reduced clear-sky downward longwave radiation reaching the surface, hence contributing to additional SST cooling in the subpolar North Atlantic (Fig. 2A, top row, T5). The maximum loading of the AMOC's imprint on clear-sky downward longwave radiation at the surface is observed over the subpolar North Atlantic and the eastern subpolar gyre, with a lag of 3 years, where a 1-Sv AMOC change is followed by a 0.22-K SST change (fig. S3, T5). This AMOC fingerprint on atmospheric radiative processes is also seen in the warm blob models (Fig. 4A, bottom row, T5). Consequently,

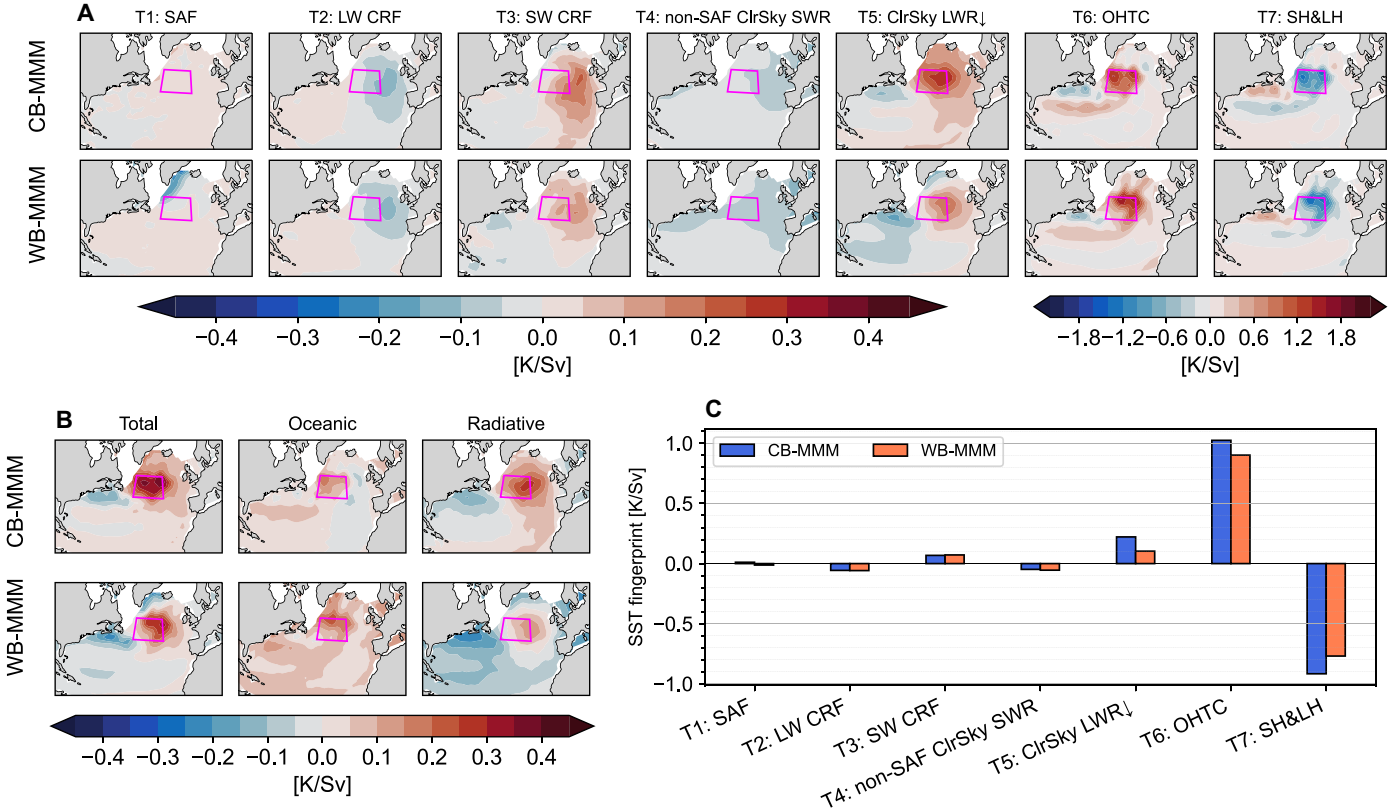

Fig. 4. The estimated fingerprints of the AMOC on SSTs through different physical processes. (**A**) The CB-MMMs (top row) and WB-MMMs (bottom row) of the decomposed SST anomalies regressed on the AMOC index anomalies (see Materials and Methods; unit: K/Sv). From left to right are the SST anomalies associated with one Sverdrup of AMOC change induced by the surface albedo feedback (T1), surface longwave cloud radiative forcing (T2), surface shortwave cloud radiative forcing (T3), surface clear-sky downward shortwave irradiance (T4), surface clear-sky downward longwave irradiance (T5), ocean heat transport convergence (T6), and surface latent heat and sensible heat fluxes (T7). (**B**) From left to right are the sum of all terms (total), the sum of T6 and T7 (oceanic), and the sum of T2, T3, T4, and T5 (radiative). (**C**) The subpolar North Atlantic regional means of the regressed SST anomalies.

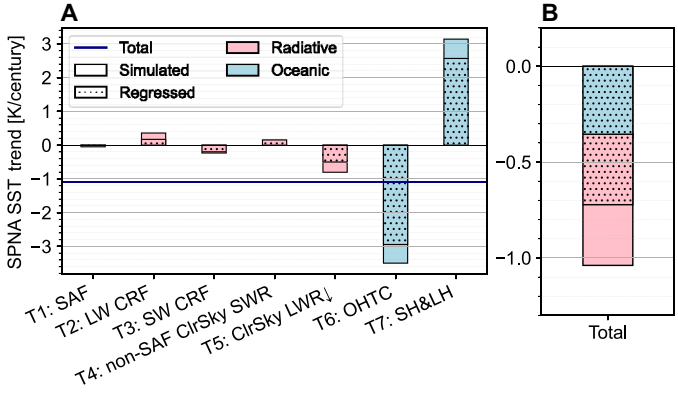

Fig. 5. CB-MMM minus WB-MMM differences in the subpolar North Atlantic regional mean SST trends. (**A**) The subpolar North Atlantic regional means of partial temperature changes, with radiative terms (T2 to T5) and oceanic terms (T6 and T7) shown by pink and blue bars, respectively. The total SST trend is indicated by the dark blue line. (**B**) Sums of the radiative terms (pink) and the oceanic terms (blue) in (A). The stippling in (A) and (B) represents the corresponding partial temperature changes obtained from the AMOC regression or, in other words, the portion of the temperature changes that is explainable by the AMOC trend.

AMOC-associated clear-sky downward longwave radiation processes explain an SST change difference of −0.49 K/century in the subpolar North Atlantic (Fig. 2D, T5).

The AMOC imprint on clear-sky downward longwave radiation suggests that the impact of AMOC variability is not limited to the surface (Fig. 6 and figs. S5 and S6). As indicated by the lag regression of subpolar North Atlantic air temperature trends on the AMOC index trend, cooling associated with a weakened AMOC occurs from the surface up to the mid-troposphere (~600 hPa), with a weak, insignificant warming in the higher troposphere (Fig. 6A). This pattern of lower troposphere cooling and upper troposphere warming is consistent with projected atmospheric responses to a collapsed AMOC (*40*). An AMOC fingerprint is also evident in atmospheric moisture, with a weakened AMOC accompanied by a decrease in lower tropospheric specific humidity (Fig. 6B) and column-integrated water vapor content (Fig. 6C) over the subpolar North Atlantic. Both the air temperature and water vapor imprints stem from sea surface responses to the AMOC decline. As the ocean surface cools due to OHTC reductions, the ocean losses less heat to the atmosphere via sensible and latent heat fluxes. The reduced heat fluxes and associated reduction in evaporation create cooler and drier atmospheric conditions that penetrate from the surface

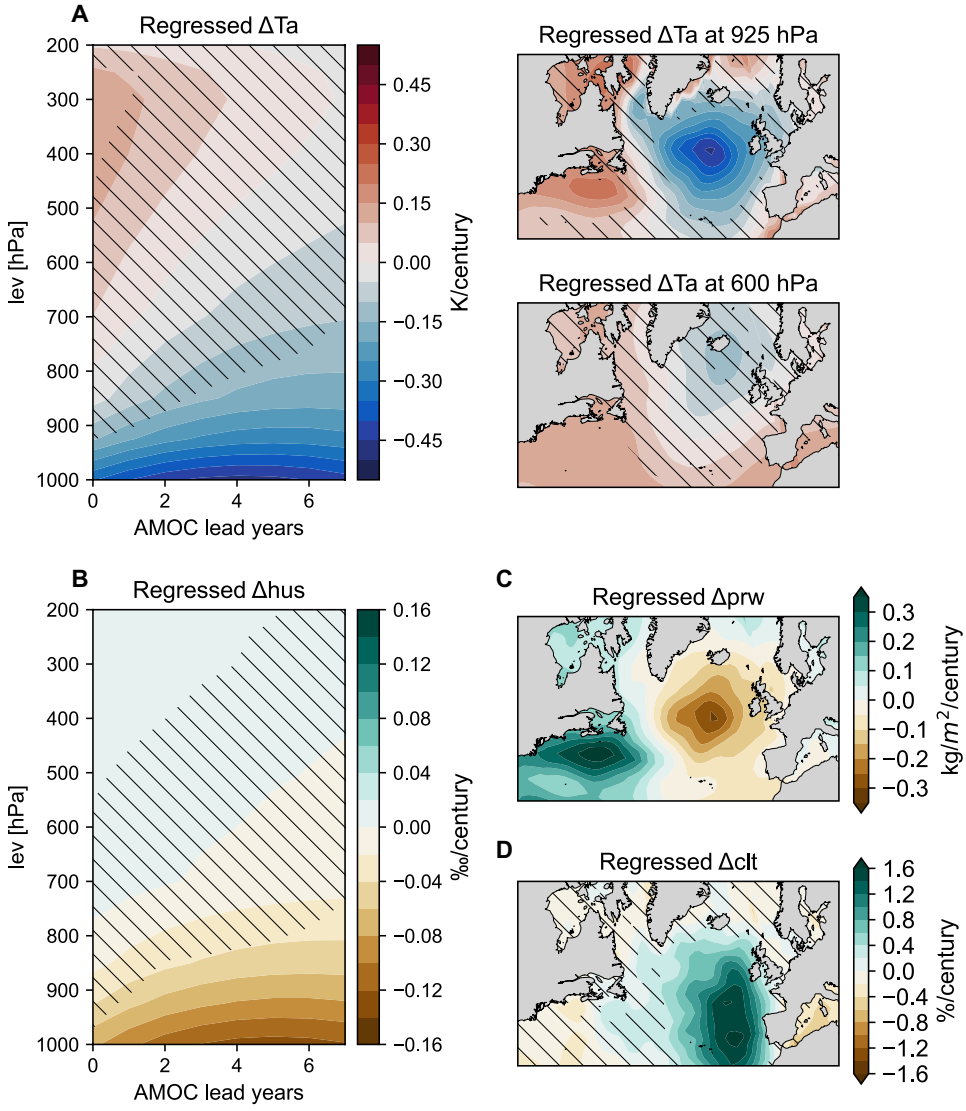

Fig. 6. CB-MMM minus WB-MMM differences in AMOC's imprint on the atmosphere. (**A**) Subpolar North Atlantic domain mean air temperature trends (Δ*Ta*; unit: K/century) regressed on the AMOC index trend. Left: Subpolar North Atlantic domain mean air temperature trends regressed on AMOC index trends with the AMOC leading the air temperature by different numbers of years. Right: The regressed trends at 925 and 500 hPa when the AMOC leads by 3 years. (**B**) Subpolar North Atlantic domain mean specific humidity trends (Δ*hus*; unit: ‰/century) regressed on the AMOC index trend with the AMOC leading the specific humidity by different numbers of years. (**C**) Trends in water vapor path (vertically integrated through the atmospheric column) regressed on the AMOC index trend with the AMOC leading by 3 years (Δ*prw*; unit: kg/m2/century). (**D**) Same as (C) but for trends in cloud area fraction for the whole atmospheric column (Δ*clt*; unit: %/century). The hatching indicates that the CB-MMM minus WB-MMM difference is not statistically significant at the 95% confidence level.

upward into the mid-troposphere. Because of the importance of temperature and water vapor to surface downward longwave radiation (*41*), this will translate into less clear-sky downward longwave radiation reaching the surface, thereby contributing to maintaining and enhancing cold SST anomalies. These changes in clear-sky downward longwave radiation at the surface are largely determined by AMOC-associated SST changes (*42*), and they, in turn, induce considerable SST changes, a positive feedback that amplifies the SST fingerprint of the AMOC.

These changes in the vertical temperature profile would increase the stratification and stability of the lower troposphere, favoring the formation of stratocumulus clouds over the subpolar North Atlantic (*43*). In the cold blob models, AMOC weakening is associated with an increase in cloud fraction downstream of the subpolar gyre (Fig. 6D and fig. S5D). This increased cloudiness leads to a reduction in surface downward shortwave radiation and an increase in surface downward longwave radiation. As a result, AMOC-associated longwave and shortwave cloud radiative effects largely counterbalance each other, resulting in a negligible net effect (Fig. 2D, T2 and T3). Although AMOC coupling to clouds has been previously suggested as contributing to the cold blob (*33*, *44*), we do not find clear evidence to support its role in reinforcing cold blob formation and maintenance.

In summary, the implication of changes in the AMOC to the long-term subpolar North Atlantic climate extends beyond its modulation of oceanic heat transport to its influences on atmospheric properties and their radiative effects. Our findings suggest that the

typical AMOC fingerprint on SST (*18*) results from a combination of two distinct but equally contributing mechanisms, one related to oceanic heat transport convergence and the other to atmospheric radiative processes and feedbacks.

DISCUSSION

This study addresses the physical processes responsible for the North Atlantic cold blob and the role the AMOC plays in them. In the historical simulation by an ensemble of CMIP6 models, the AMOC slowdown is largely responsible for the subpolar North Atlantic cold blob. However, unlike previous studies that emphasize the predominant effect of oceanic heat transport, our findings highlight that AMOC's contributions to the cold blob also involve a dampening effect by surface turbulent heat fluxes and an enhancing effect by surface clear-sky downward longwave radiation. In models that simulate a North Atlantic cold blob (cold blob models), the simulated AMOC decline is associated with a substantial cooling induced by a reduction in OHTC, which is almost completely (~90%) offset by adjustments in surface turbulent heat fluxes. The AMOC weakening is also associated with a reduction in surface clear-sky downward longwave radiation, which largely offsets the warming expected from increasing amounts of heat-trapping gases in the past century. On the contrary, models with accelerated warming in the subpolar North Atlantic (warm blob models) show an AMOC strengthening and associated warming from both oceanic and radiative pathways. As a result, the difference in the AMOC trend between the cold blob and warm blob models explains an SST trend difference of −0.71 K/century, with half accounted for through oceanic processes and the other half through radiative processes. Notably, the AMOC-associated changes in surface clear-sky downward longwave radiation alone are responsible for a difference of −0.49 K/century. Overall, we conclude that radiative and oceanic processes are equally important in explaining the contributions of the weakening AMOC to the simulated North Atlantic cold blob over the historical period.

This study emphasizes the radiative effects of atmospheric changes accompanying AMOC weakening, particularly lower troposphere cooling and drying. These responses feedback on the SST change via downward longwave radiation, further amplifying the preexisting SST cooling induced by oceanic processes. Consistent evidence is found in the NOAA-CIRES 20th Century Reanalysis, V2 (*45*), which shows that changes in surface downward longwave radiation induce a subpolar North Atlantic warming hole; this longwave radiation–induced warming hole is associated with a lack of temperature and moisture increase in the lower troposphere over the region (fig. S7). The atmospheric responses to AMOC changes are recognized by recent studies (*40*, *46*) and suggested to be nonlinear (*40*). This nonlinearity complicates the understanding of subpolar North Atlantic SST changes and associated climatic impacts (*9*), supporting the view that the AMOC is a major source of intermodel uncertainty in future climate change projections (*47*). Thus, understanding AMOC's impacts on atmospheric properties and their radiative effects is a valuable research avenue. Moreover, as AMOC-associated radiative effects may introduce uncertainty in SST-based reconstructions of AMOC variability, other indicators, such as salinity, might be more reliable for detecting signals of AMOC changes (*48*).

While our study provides another line of evidence supporting the role of the AMOC in driving the historical trend of subpolar North Atlantic SSTs, it is noteworthy that about one-third of the SST trend difference between the cold blob and warm blob models cannot be explained by the AMOC using our current framework (Fig. 5B, nonstippled pink box). Similarly, half of the intermodel variance in the simulated SST trend remains unexplained by a simple AMOC trend (Fig. 1F). These results suggest that factors other than AMOC variability need to be considered. One potential factor is equilibrium climate sensitivity (ECS), a global metric representing how sensitive the Earth's surface temperature is to rising carbon dioxide concentrations. Across the two groups of models, ECS explains 45% of the variance in the simulated subpolar North Atlantic SST trend ($R^2 = 0.45$). With a higher ECS, the same increase in atmospheric concentration of heat-trapping gases leads to greater surface warming. The cold blob models, on average, have an ECS of 3.0 K, whereas the warm blob models have a much higher ECS of 4.7 K (Fig. 1F), indicating weaker global warming in the cold blob models than in the warm blob models given the same historical forcing. This is consistent with a previous study suggesting a reduced ECS with the existence of the North Atlantic cold blob (*9*). Note that models with a lower ECS also tend to simulate a more negative historical trend of the AMOC (*24*). A detailed examination of the relationship among ECS, the AMOC trend, and North Atlantic SST trends is an important future undertaking.

This study investigates the physical processes linking AMOC to the North Atlantic cold blob in historical simulations from multiple state-of-the-art global climate models. Our diagnosis pinpoints the AMOC slowdown as the primary driver of the cold blob, with roughly equal contributions from oceanic and atmospheric processes. A key implication is that clear-sky longwave radiation feedback has considerable contribution to the formation and maintenance of the cold blob, a process not yet fully recognized. Despite these insights, model spread remains in representing AMOC mean state and variability (*24*). For example, models with stronger anthropogenic aerosol forcing tend to simulate more strengthening of the AMOC over the historical period, likely inconsistent with observations (*49*). Future climate projection in the subpolar North Atlantic relies on the evolution of the AMOC, as well as the oceanic and atmospheric responses to it, both of which are dependent on the base-state AMOC itself (*50*, *51*). Thus, continuous observations of the AMOC and appropriate methods e.g., (*52*) are needed to constrain model simulations and to yield a more reliable projection for the subpolar North Atlantic.

MATERIALS AND METHODS

Observational SST datasets

Three century-long global SST datasets are used in this study: the Hadley Centre SST (*53*), the Extended Reconstructed SST Version 5 (*54*), and the Kaplan Extended SST Version 2 (*55*). SST anomalies are referenced to the period from 1951 to 1980 to maintain consistency with the period used in the original Kaplan dataset. All three datasets agree on the century-long SST cooling trend southeast of Greenland (fig. S1A), a phenomenon referred to as the North Atlantic cold blob. The magnitude of the observed cold blob is quantified by the SST trend averaged over the domain from 25°W-45°W to 50°N-60°N centered on the cooling. We acknowledge uncertainties in estimating the magnitude of the observed cold blob, as seen from differences across the three datasets (fig. S1B). Even though the choice of datasets does not affect the main conclusions of our study, we use the mean of the three datasets as an estimate of the observed SST trends.

CMIP6 simulations and model selection

This study uses output from the 165-year (1850–2014) full-forcing historical experiments compiled under the CMIP6 protocol. Among the 32 CMIP6 models examined, the 11 models that simulate an SST cooling trend in the subpolar North Atlantic are chosen as the cold blob models: CMCC-CM2-SR5, CMCC-ESM2, FGOALS-f3-L, FGOALS-g3, GFDL-ESM4, GISS-E2-1-G, GISS-E3-G, INM-CM4-8, MPI-ESM1-2-HR, MPI-ESM1-2-LR, and SAM0-UNICON. As a counterpart group, nine models that simulate more warming than elsewhere in the North Atlantic are selected as the warm blob models: CanESM5, CESM2, CESM2-WACCM, CESM2-FV2, CESM2-WACCM-FV2, EC-Earth3-AerChem, IPSL-CM6A-LR-INCA, IPSL-CM6A-LR, and MRI-ESM2-0 (fig. S2). The remaining CMIP6 models are not included in our analysis because they either simulate statistically insignificant SST trends in the subpolar North Atlantic over the period from 1900 to 2014 or their archived output does not include variables required for the analysis. Model information is summarized in table S1. The ECS of these models is based on calculations in previous studies (*56*, *57*).

AMOC index

The AMOC is commonly defined as the zonally and vertically integrated northward volume transport in the Atlantic basin, thus a function of latitude and depth, with the unit of cubic meter per second, or more commonly, Sverdrup (1 Sv $\equiv 10^6$ m^3 s^{-1}). In this study, we use direct CMIP6 output of the Atlantic overturning mass stream function to represent the AMOC, which corresponds to its common definition if multiplied by the density of seawater (e.g., 10^9 kg s^{-1} =1 Sv assuming the density of seawater is 1000 kg m^{-3}). The strength of the two-dimensional AMOC is generally represented by an AMOC index, defined as the maximum of the Atlantic overturning mass stream function from 10°N to 90°N and below the depth of 500 m. On decadal and longer timescales, the subtropical and subpolar AMOC estimates are coherent (*58*). The AMOC index as defined is intended to capture overturning circulation variability that is meaningful to the subpolar North Atlantic heat balance.

SST trend decomposition

The time tendency of annual mean ocean heat content (*OHC*) within the whole-depth water column is determined by the net downward heat flux at the surface (Q) and ocean heat transport (*OHT*) convergence in the horizontal direction

$$\frac{\partial OHC}{\partial t} = Q + (-\nabla \cdot \boldsymbol{OHT}) \tag{1}$$

On timescales longer than 25 years, the magnitude of $\frac{\partial OHC}{\partial t}$ is generally one magnitude smaller than Q in the subpolar North Atlantic (e.g., 25°W-45°W, 45°N-55°N). Therefore, $\frac{\partial OHC}{\partial t} \approx 0$, and Q has to be largely balanced by $\nabla \cdot \boldsymbol{OHT}$ on multidecadal timescales. We thus infer that $-\nabla \cdot \boldsymbol{OHT}$, namely, the OHT convergence (OHTC), is the residual of Eq. 1 as $-\nabla \cdot \boldsymbol{OHT} \approx -Q$, which is a common approach to estimate OHT effects (*59*).

The net surface downward heat flux, Q, can be expanded as the sum of surface downward shortwave irradiance ()$SW^{\downarrow}$ absorbed by the surface with an albedo α, downward longwave irradiance ($LW^{\downarrow}$), upward surface sensible heat (SH) and latent heat (LH) fluxes, and upward longwave irradiance ($LW^{\uparrow}$)

$$Q = (1-\alpha)SW^{\downarrow} + LW^{\downarrow} - (SH+LH) - LW^{\uparrow} \tag{2}$$

Under the assumption that seawater is approximately a black body in the infrared with an emissivity close to 1, $LW^{\uparrow}$can be expressed as σT^4, where σ is the Stefan-Boltzmann constant and T is the surface temperature. As clouds influence downward longwave and shortwave irradiance, we further account for cloud radiative forcing (CRF) as $LW^{\downarrow} = LW^{\downarrow CRF} + LW^{\downarrow(clear-sky)}$ and $SW^{\downarrow} = SW^{\downarrow CRF} + SW^{\downarrow(clear-sky)}$, where $()^{\downarrow(\text{clear-sky})}$ is surface downward irradiance assuming a clear sky. Taking the linear trend of each term in Eq. 2 yields

$$\begin{aligned}\Delta Q = \Delta\left\{(1-\alpha)\left[SW^{\downarrow CRF} + SW^{\downarrow(\text{clear-sky})}\right]\right\} + \\ \Delta\left[LW^{\downarrow CRF} + LW^{\downarrow(clear-sky)}\right] - \Delta(SH+LH) - \Delta\left(\sigma T^4\right)\end{aligned} \tag{3}$$

We linearize Eq. 3 by setting

$$\Delta LW^{\uparrow} = 4\sigma\overline{T}^3\,\Delta T$$

$$\Delta\left(\alpha SW^{\downarrow CRF}\right) = \overline{\alpha}\Delta SW^{\downarrow CRF} + \Delta\alpha\overline{SW^{\downarrow CRF}} + \Delta\alpha\Delta SW^{\downarrow CRF}$$

and

$$\begin{aligned}\Delta[\alpha SW^{\downarrow(clear-sky)}] = \overline{\alpha}\Delta SW^{\downarrow(clear-sky)} + \\ \Delta\alpha\overline{SW^{\downarrow(clear-sky)}} + \Delta\alpha\Delta SW^{\downarrow(clear-sky)}\end{aligned}$$

where $\overline{()}$ represents the climatology over the period from 1900 to 2014 of any variable. Eq. 3 then becomes

$$\begin{aligned}\Delta Q = -\Delta\alpha\overline{SW^{\downarrow}} - \Delta\alpha\Delta SW^{\downarrow} + (1-\overline{\alpha})\Delta SW^{\downarrow CRF} + \\ (1-\overline{\alpha})\Delta SW^{\downarrow(clear-sky)} + \Delta LW^{\downarrow(CRF)} + \Delta LW^{\downarrow(clear-sky)} - \\ \Delta(SH+LH) - 4\sigma\overline{T}^3\Delta T\end{aligned} \tag{4}$$

Rearranging the terms in Eq. 4, substituting $-Q$ with $-\nabla \cdot \boldsymbol{OHT}$ based on Eq. 1, and dividing each term by $4\sigma\overline{T}^3$, we arrive at the decomposition of the surface temperature change into partial temperature changes related to different physical processes

$$\begin{aligned}\Delta T = \frac{1}{4\sigma\overline{T}^3}\Big[-\Delta\alpha\left(\overline{SW^{\downarrow}} + \Delta SW^{\downarrow}\right) + \Delta LW^{\downarrow(CRF)} + \\ (1-\overline{\alpha})\Delta SW^{\downarrow(CRF)} + (1-\overline{\alpha})\Delta SW^{\downarrow(clear-sky)} + \Delta LW^{\downarrow(clear-sky)} + \\ \Delta(-\nabla \cdot \boldsymbol{OHT}) - \Delta(SH+LH)\Big]\end{aligned} \tag{5}$$

The seven processes, represented by the seven terms within the brackets, are the (i) surface albedo feedback (SAF) change, (ii) LW CRF change, (iii) SW CRF change, (iv) non–SAF-induced change in clear-sky SW, (v) clear-sky downward longwave radiation change, (vi) OHT convergence change, and (vii) surface turbulent heat flux change, respectively. All variables in Eq. 5 are direct outputs from the cold blob and warm blob models, except for the surface albedo, which we calculate as the ratio of surface upward shortwave irradiance to surface downward shortwave irradiance at each grid point $\left(\alpha = \frac{SW^{\uparrow}}{SW^{\downarrow}}\right)$. The differences between the sum of all partial temperature changes and the simulated SST changes are negligible in the North Atlantic open ocean (fig. S8), demonstrating the validity of

this decomposition method. Similar decomposition methods have been used in previous studies to address the mechanisms for Arctic surface warming and North Atlantic surface cooling (*60*, *61*).

Lagged regression analysis

We use the least-squares fitting method to estimate the partial temperature changes, as well as air temperature and water vapor concentration changes, that are attributable to changes in AMOC. To this end, we use the equation

$$\Delta F = \frac{\partial F}{\partial AMOC}\Delta AMOC + residual \quad (6)$$

where $\frac{\partial F}{\partial AMOC}$ denotes sensitivity of surface heat flux F (e.g., surface turbulent heat flux) to the AMOC index change, and the residual represents the changes in F that are irrelevant to the AMOC. The sensitivity is estimated by linear regression of the variable F on the AMOC index, with the AMOC index leading by N years ($N \geq 0$). The time series is detrended and 9-year smoothed before the regression. Here, detrending aims to remove any linear relationship between F and the AMOC index that might result from the response of the two variables to external forcing, a confounding factor. Nine-year smoothing is applied to reduce the effect of high-frequency variability and to emphasize the AMOC-SST coupling on decadal timescales. The N-year lag accounts for potential time differences between anomalies in the AMOC strength and variable F. We acknowledge that decadal AMOC variability might, in turn, be influenced by surface heat fluxes in some regions, such as the Labrador Sea (*62*), and not others. Our regression approach here only aims to estimate the potential influence of the AMOC change on surface heat fluxes, rather than the other way around. Thus, we perform the regression with the AMOC always leading the heat flux by some number of years, subsequently focusing on the lag time that maximizes the absolute value of the regression coefficient in the subpolar North Atlantic domain. Specifically, the 2-year, 3-year, 2-year, 0-year, 3-year, 2-year, and 2-year lags lead to the regression coefficients with the largest magnitude in the region of interest for the seven terms, respectively (fig. S3). We calculate the regression for each model, and then take the ensemble means as the final regression estimate for the CB and WB models, respectively.

Significance test

The statistical significance of the CB-MMM minus WB-MMM differences in SST changes is estimated by bootstrapping. For each grid point and each term, we randomly draw a resample of size 11 from SST change from the cold blob models and a resample of size 9 from the warm blob models, and then calculate the difference between the multimodel mean of the two resample. After resampling for 1000 times, we can estimate a distribution of the difference. The difference is considered as statistically significant at the 95% confidence level if the 95th percentile of the estimated distribution of the difference is larger or smaller than zero, depending on the sign of the sample mean difference.

Supplementary Materials

This PDF file includes:

Figs. S1 to S8
Table S1
References

REFERENCES AND NOTES

1. Intergovernmental Panel on Climate Change (IPCC), "Framing and Context" in *Global Warming of 1.5°C: IPCC Special Report on Impacts of Global Warming of 1.5°C above Pre-Industrial Levels in Context of Strengthening Response to Climate Change, Sustainable Development, and Efforts to Eradicate Poverty* (Cambridge Univ. Press, 2022), pp. 49–92.
2. L. Li, M. S. Lozier, F. Li, Century-long cooling trend in subpolar North Atlantic forced by atmosphere: An alternative explanation. *Climate Dyn.* **58**, 2249–2267 (2022).
3. Y. Fan, W. Liu, P. Zhang, R. Chen, L. Li, North Atlantic Oscillation contributes to the subpolar North Atlantic cooling in the past century. *Climate Dyn.* **61**, 5199–5215 (2023).
4. S. Drijfhout, G. J. van Oldenborgh, A. Cimatoribus, Is a decline of AMOC causing the warming hole above the North Atlantic in observed and modeled warming patterns? *J. Clim.* **25**, 8373–8379 (2012).
5. H. Kim, S.-I. An, On the subarctic North Atlantic cooling due to global warming. *Theor. Appl. Climatol.* **114**, 9–19 (2013).
6. L. Caesar, S. Rahmstorf, A. Robinson, G. Feulner, V. Saba, Observed fingerprint of a weakening Atlantic Ocean overturning circulation. *Nature* **556**, 191–196 (2018).
7. S. Rahmstorf, J. E. Box, G. Feulner, M. E. Mann, A. Robinson, S. Rutherford, E. J. Schaffernicht, Exceptional twentieth-century slowdown in Atlantic Ocean overturning circulation. *Nat. Clim. Change* **5**, 475–480 (2015).
8. M. Winton, S. M. Griffies, B. L. Samuels, J. L. Sarmiento, T. L. Frölicher, Connecting changing ocean circulation with changing climate. *J. Clim.* **26**, 2268–2278 (2013).
9. I. Mitevski, Y. Dong, L. M. Polvani, M. Rugenstein, C. Orbe, Non-monotonic feedback dependence under abrupt CO_2 forcing due to a North Atlantic pattern effect. *Geophys. Res. Lett.* **50**, e2023GL103617 (2023).
10. T. Woollings, J. M. Gregory, J. G. Pinto, M. Reyers, D. J. Brayshaw, Response of the North Atlantic storm track to climate change shaped by ocean–Atmosphere coupling. *Nat. Geosci.* **5**, 313–317 (2012).
11. R. J. Haarsma, F. M. Selten, S. S. Drijfhout, Decelerating Atlantic meridional overturning circulation main cause of future west European summer atmospheric circulation changes. *Environ. Res. Lett.* **10**, 094007 (2015).
12. M. Gervais, J. Shaman, Y. Kushnir, Impact of the North Atlantic warming hole on sensible weather. *J. Clim.* **33**, 4255–4271 (2020).
13. K. B. Karnauskas, L. Zhang, D. J. Amaya, The atmospheric response to North Atlantic SST trends, 1870–2019. *Geophys. Res. Lett.* **48**, e2020GL090677 (2021).
14. X. Ren, W. Liu, The role of a weakened Atlantic meridional overturning circulation in modulating marine heatwaves in a warming climate. *Geophys. Res. Lett.* **48**, e2021GL095941 (2021).
15. C. M. Free, J. T. Thorson, M. L. Pinsky, K. L. Oken, J. Wiedenmann, O. P. Jensen, Impacts of historical warming on marine fisheries production. *Science* **363**, 979–983 (2019).
16. Y. Fu, F. Li, J. Karstensen, C. Wang, A stable Atlantic meridional overturning circulation in a changing North Atlantic Ocean since the 1990s. *Sci. Adv.* **6**, eabc7836 (2020).
17. K. H. Kilbourne, A. D. Wanamaker, P. Moffa-Sanchez, D. J. Reynolds, D. E. Amrhein, P. G. Butler, G. Gebbie, M. Goes, M. F. Jansen, C. M. Little, M. Mette, E. Moreno-Chamarro, P. Ortega, B. L. Otto-Bliesner, T. Rossby, J. Scourse, N. M. Whitney, Atlantic circulation change still uncertain. *Nat. Geosci.* **15**, 165–167 (2022).
18. R. Zhang, Coherent surface-subsurface fingerprint of the Atlantic meridional overturning circulation. *Geophys. Res. Lett.* **35**, L20705 (2008).
19. R. Zhang, R. Sutton, G. Danabasoglu, Y. Kwon, R. Marsh, S. G. Yeager, D. E. Amrhein, C. M. Little, A review of the role of the Atlantic meridional overturning circulation in Atlantic multidecadal variability and associated climate impacts. *Rev. Geophys.* **57**, 316–375 (2019).
20. C. D. Roberts, F. K. Garry, L. C. Jackson, A multimodel study of sea surface temperature and subsurface density fingerprints of the Atlantic meridional overturning circulation. *J. Climate* **26**, 9155–9174 (2013).
21. W. Liu, A. V. Fedorov, S.-P. Xie, S. Hu, Climate impacts of a weakened Atlantic meridional overturning circulation in a warming climate. *Sci. Adv.* **6**, eaaz4876 (2020).
22. J. Lynch-Stieglitz, The Atlantic meridional overturning circulation and abrupt climate change. *Ann. Rev. Mar. Sci.* **9**, 83–104 (2017).
23. R. B. Alley, A. M. Ágústsdóttir, The 8k event: Cause and consequences of a major Holocene abrupt climate change. *Quat. Sci. Rev.* **24**, 1123–1149 (2005).
24. W. Weijer, W. Cheng, O. A. Garuba, A. Hu, B. T. Nadiga, CMIP6 models predict significant 21st century decline of the Atlantic meridional overturning circulation. *Geophys. Res. Lett.* **47**, e2019GL086075 (2020).
25. M. W. Buckley, J. Marshall, Observations, inferences, and mechanisms of the Atlantic meridional overturning circulation: A review. *Rev. Geophys.* **54**, 5–63 (2016).
26. M. B. Menary, R. A. Wood, An anatomy of the projected North Atlantic warming hole in CMIP5 models. *Clim. Dyn.* **50**, 3063–3080 (2018).
27. L. Li, M. S. Lozier, M. W. Buckley, An investigation of the ocean's role in Atlantic multidecadal variability. *J. Clim.* **33**, 3019–3035 (2020).

28. R. J. Small, F. O. Bryan, S. P. Bishop, S. Larson, R. A. Tomas, What drives upper-ocean temperature variability in coupled climate models and observations? *J. Clim.* **33**, 577–596 (2020).
29. A. Clement, K. Bellomo, L. N. Murphy, M. A. Cane, T. Mauritsen, G. Rädel, B. Stevens, The Atlantic multidecadal oscillation without a role for ocean circulation. *Science* **350**, 320–324 (2015).
30. G. Liu, Y.-O. Kwon, C. Frankignoul, J. Lu, Understanding the drivers of Atlantic multidecadal variability using a stochastic model hierarchy. *J. Clim.* **36**, 1043–1058 (2023).
31. B. B. B. Booth, N. J. Dunstone, P. R. Halloran, T. Andrews, N. Bellouin, Aerosols implicated as a prime driver of twentieth-century North Atlantic climate variability. *Nature* **484**, 228–232 (2012).
32. T. L. Delworth, F. Zeng, L. Zhang, R. Zhang, G. A. Vecchi, X. Yang, The central role of ocean dynamics in connecting the North Atlantic oscillation to the extratropical component of the Atlantic multidecadal oscillation. *J. Clim.* **30**, 3789–3805 (2017).
33. P. Keil, T. Mauritsen, J. Jungclaus, C. Hedemann, D. Olonscheck, R. Ghosh, Multiple drivers of the North Atlantic Warming hole. *Nat. Clim. Change* **10**, 667–671 (2020).
34. C. He, A. C. Clement, M. A. Cane, L. N. Murphy, J. M. Klavans, T. M. Fenske, A North Atlantic warming hole without ocean circulation. *Geophys. Res. Lett.* **49**, e2022GL100420 (2022).
35. V. Eyring, S. Bony, G. A. Meehl, C. A. Senior, B. Stevens, R. J. Stouffer, K. E. Taylor, Overview of the Coupled Model Intercomparison Project Phase 6 (CMIP6) experimental design and organization. *Geosci. Model Dev.* **9**, 1937–1958 (2016).
36. S. K. Gulev, M. Latif, N. Keenlyside, W. Park, K. P. Koltermann, North Atlantic Ocean control on surface heat flux on multidecadal timescales. *Nature* **499**, 464–467 (2013).
37. U. Hausmann, A. Czaja, J. Marshall, Mechanisms controlling the SST air-sea heat flux feedback and its dependence on spatial scale. *Clim. Dyn.* **48**, 1297–1307 (2017).
38. M. Klockmann, U. Mikolajewicz, H. Kleppin, J. Marotzke, Coupling of the subpolar gyre and the overturning circulation during abrupt glacial climate transitions. *Geophys. Res. Lett.* **47**, e2020GL090361 (2020).
39. D. Swingedouw, P. Braconnot, P. Delecluse, E. Guilyardi, O. Marti, Quantifying the AMOC feedbacks during a 2×CO_2 stabilization experiment with land-ice melting. *Clim. Dyn.* **29**, 521–534 (2007).
40. C. Orbe, D. Rind, R. L. Miller, L. S. Nazarenko, A. Romanou, J. Jonas, G. L. Russell, M. Kelley, G. A. Schmidt, Atmospheric response to a collapse of the North Atlantic circulation under a mid-range future climate scenario: A regime shift in northern hemisphere dynamics. *J. Clim.* **36**, 6669–6693 (2023).
41. J. P. Clark, E. E. Clothiaux, S. B. Feldstein, S. Lee, Drivers of global clear sky surface downwelling longwave irradiance trends from 1984 to 2017. *Geophys. Res. Lett.* **48**, e2021GL093961 (2021).
42. L. R. Vargas Zeppetello, A. Donohoe, D. S. Battisti, Does surface temperature respond to or determine downwelling longwave radiation? *Geophys. Res. Lett.* **46**, 2781–2789 (2019).
43. S. A. Klein, D. L. Hartmann, The seasonal cycle of low stratiform clouds. *J. Clim.* **6**, 1587–1606 (1993).
44. D. S. Trossman, J. B. Palter, T. M. Merlis, Y. Huang, Y. Xia, Large-scale ocean circulation-cloud interactions reduce the pace of transient climate change. *Geophys. Res. Lett.* **43**, 3935–3943 (2016).
45. G. P. Compo, J. S. Whitaker, P. D. Sardeshmukh, N. Matsui, R. J. Allan, X. Yin, B. E. Gleason, R. S. Vose, G. Rutledge, P. Bessemoulin, S. Brönnimann, M. Brunet, R. I. Crouthamel, A. N. Grant, P. Y. Groisman, P. D. Jones, M. C. Kruk, A. C. Kruger, G. J. Marshall, M. Maugeri, H. Y. Mok, Ø. Nordli, T. F. Ross, R. M. Trigo, X. L. Wang, S. D. Woodruff, S. J. Worley, The twentieth century reanalysis project. *Q. J. Roy. Meteorol. Soc.* **137**, 1–28 (2011).
46. B. Orihuela-Pinto, M. H. England, A. S. Taschetto, Interbasin and interhemispheric impacts of a collapsed Atlantic overturning circulation. *Nat. Clim. Change* **12**, 558–565 (2022).
47. K. Bellomo, M. Angeloni, S. Corti, J. von Hardenberg, Future climate change shaped by inter-model differences in Atlantic meridional overturning circulation response. *Nat. Commun.* **12**, 3659 (2021).
48. C. Zhu, Z. Liu, S. Zhang, L. Wu, Likely accelerated weakening of Atlantic overturning circulation emerges in optimal salinity fingerprint. *Nat. Commun.* **14**, 1245 (2023).
49. J. Robson, M. B. Menary, R. T. Sutton, J. Mecking, J. M. Gregory, C. Jones, B. Sinha, D. P. Stevens, L. J. Wilcox, The role of anthropogenic aerosol forcing in the 1850–1985 strengthening of the AMOC in CMIP6 historical simulations. *J. Clim.* **35**, 3243–3263 (2022).
50. L. C. Jackson, M. J. Roberts, H. T. Hewitt, D. Iovino, T. Koenigk, V. L. Meccia, C. D. Roberts, Y. Ruprich-Robert, R. A. Wood, Impact of ocean resolution and mean state on the rate of AMOC weakening. *Clim. Dyn.* **55**, 1711–1732 (2020).
51. Y.-J. Lin, B. E. J. Rose, Y.-T. Hwang, Mean state AMOC affects AMOC weakening through subsurface warming in the Labrador Sea. *J. Clim.* **36**, 3895–3915 (2023).
52. S. Qasmi, Past and Future response of the North Atlantic warming hole to anthropogenic forcing. *Earth Syst. Dyn.* **14**, 685–695 (2023).
53. N. A. Rayner, D. E. Parker, E. B. Horton, C. K. Folland, L. V. Alexander, D. P. Rowell, E. C. Kent, A. Kaplan, Global analyses of sea surface temperature, sea ice, and night marine air temperature since the late nineteenth century. *J. Geophys. Res. Atmos.* **108**, 4407 (2003).
54. B. Huang, P. W. Thorne, V. F. Banzon, T. Boyer, G. Chepurin, J. H. Lawrimore, M. J. Menne, T. M. Smith, R. S. Vose, H.-M. Zhang, Extended reconstructed sea surface temperature, version 5 (ERSSTv5): Upgrades, validations, and intercomparisons. *J. Clim.* **30**, 8179–8205 (2017).
55. A. Kaplan, M. A. Cane, Y. Kushnir, A. C. Clement, M. B. Blumenthal, B. Rajagopalan, Analyses of global sea surface temperature 1856-1991. *J. Geophys. Res. Oceans* **103**, 18567–18589 (1998).
56. G. A. Meehl, C. A. Senior, V. Eyring, G. Flato, J.-F. Lamarque, R. J. Stouffer, K. E. Taylor, M. Schlund, Context for interpreting equilibrium climate sensitivity and transient climate response from the CMIP6 Earth system models. *Sci. Adv.* **6**, eaba1981 (2020).
57. N. Scafetta, Advanced testing of low, medium, and high ECS CMIP6 GCM simulations versus ERA5-T2m. *Geophys. Res. Lett.* **49**, e2022GL097716 (2022).
58. S. Gu, Z. Liu, L. Wu, Time scale dependence of the meridional coherence of the Atlantic meridional overturning circulation. *J. Geophys. Res. Oceans* **125**, e2019JC015838 (2020).
59. S.-P. Xie, C. Deser, G. A. Vecchi, J. Ma, H. Teng, A. T. Wittenberg, Global warming pattern formation: Sea surface temperature and rainfall. *J. Clim.* **23**, 966–986 (2010).
60. S. Lee, T. Gong, S. B. Feldstein, J. A. Screen, I. Simmonds, Revisiting the cause of the 1989–2009 Arctic surface warming using the surface energy budget: Downward infrared radiation dominates the surface fluxes. *Geophys. Res. Lett.* **44**, 10654–10661 (2017).
61. Y. Fan, J. Lu, L. Li, Mechanism of the centennial subpolar North Atlantic cooling trend in the FGOALS-g2 historical simulation. *J. Geophys. Res. Oceans* **126**, e2021JC017511 (2021).
62. D. Stephenson, D. E. Amrhein, L. Thompson, Three atmospheric patterns dominate decadal North Atlantic overturning variability. *Geophys. Res. Lett.* **51**, e2024GL109193 (2024).
63. A. Cherchi, P. G. Fogli, T. Lovato, D. Peano, D. Iovino, S. Gualdi, S. Masina, E. Scoccimarro, S. Materia, A. Bellucci, A. Navarra, Global mean climate and main patterns of variability in the CMCC-CM2 coupled model. *J. Adv. Model. Earth Syst.* **11**, 185–209 (2019).
64. T. Lovato, D. Peano, M. Butenschön, S. Materia, D. Iovino, E. Scoccimarro, P. G. Fogli, A. Cherchi, A. Bellucci, S. Gualdi, S. Masina, A. Navarra, CMIP6 simulations with the CMCC Earth System Model (CMCC-ESM2). *J. Adv. Model. Earth Syst.* **14**, e2021MS002814 (2022).
65. J. P. Dunne, L. W. Horowitz, A. J. Adcroft, P. Ginoux, I. M. Held, J. G. John, J. P. Krasting, S. Malyshev, V. Naik, F. Paulot, E. Shevliakova, C. A. Stock, N. Zadeh, V. Balaji, C. Blanton, K. A. Dunne, C. Dupuis, J. Durachta, R. Dussin, P. P. G. Gauthier, S. M. Griffies, H. Guo, R. W. Hallberg, M. Harrison, J. He, W. Hurlin, C. McHugh, R. Menzel, P. C. D. Milly, S. Nikonov, D. J. Paynter, J. Ploshay, A. Radhakrishnan, K. Rand, B. G. Reichl, T. Robinson, D. M. Schwarzkopf, L. T. Sentman, S. Underwood, H. Vahlenkamp, M. Winton, A. T. Wittenberg, B. Wyman, Y. Zeng, M. Zhao, The GFDL Earth System Model Version 4.1 (GFDL-ESM 4.1): Overall coupled model description and simulation characteristics. *J. Adv. Model. Earth Syst.* **12**, e2019MS002015 (2020).
66. M. Kelley, G. A. Schmidt, L. S. Nazarenko, S. E. Bauer, R. Ruedy, G. L. Russell, A. S. Ackerman, I. Aleinov, M. Bauer, R. Bleck, V. Canuto, G. Cesana, Y. Cheng, T. L. Clune, B. I. Cook, C. A. Cruz, A. D. Del Genio, G. S. Elsaesser, G. Faluvegi, N. Y. Kiang, D. Kim, A. A. Lacis, A. Leboissetier, A. N. LeGrande, K. K. Lo, J. Marshall, E. E. Matthews, S. McDermid, K. Mezuman, R. L. Miller, L. T. Murray, V. Oinas, C. Orbe, C. P. García-Pando, J. P. Perlwitz, M. J. Puma, D. Rind, A. Romanou, D. T. Shindell, S. Sun, N. Tausnev, K. Tsigaridis, G. Tselioudis, E. Weng, J. Wu, M.-S. Yao, GISS-E2.1: Configurations and Climatology. *J. Adv. Model. Earth Syst.* **12**, e2019MS002025 (2020).
67. B. He, Y. Liu, G. Wu, Q. Bao, T. Zhou, X. Wu, L. Wang, J. Li, X. Wang, J. Li, W. Hu, X. Zhang, C. Sheng, Y. Tang, CAS FGOALS-f3-L model datasets for CMIP6 GMMIP tier-1 and tier-3 experiments. *Adv. Atmos. Sci.* **37**, 18–28 (2020).
68. E. M. Volodin, E. V. Mortikov, S. V. Kostrykin, V. Y. Galin, V. N. Lykossov, A. S. Gritsun, N. A. Diansky, A. V. Gusev, N. G. Iakovlev, A. A. Shestakova, S. V. Emelina, Simulation of the modern climate using the INM-CM48 climate model. *Russ. J. Numer. Anal. Math. Model.* **33**, 367–374 (2018).
69. W. A. Müller, J. H. Jungclaus, T. Mauritsen, J. Baehr, M. Bittner, R. Budich, F. Bunzel, M. Esch, R. Ghosh, H. Haak, T. Ilyina, T. Kleine, L. Kornblueh, H. Li, K. Modali, D. Notz, H. Pohlmann, E. Roeckner, I. Stemmler, F. Tian, J. Marotzke, A higher-resolution version of the Max Planck Institute Earth System Model (MPI-ESM1.2-HR). *J. Adv. Model. Earth Syst.* **10**, 1383–1413 (2018).
70. S. Park, J. Shin, S. Kim, E. Oh, Y. Kim, Global climate simulated by the Seoul National University Atmosphere Model Version 0 with a Unified Convection Scheme (SAM0-UNICON). *J. Clim.* **32**, 2917–2949 (2019).
71. N. C. Swart, J. N. S. Cole, V. V. Kharin, M. Lazare, J. F. Scinocca, N. P. Gillett, J. Anstey, V. Arora, J. R. Christian, S. Hanna, Y. Jiao, W. G. Lee, F. Majaess, O. A. Saenko, C. Seiler, C. Seinen, A. Shao, M. Sigmond, L. Solheim, K. von Salzen, D. Yang, B. Winter, The Canadian Earth System Model version 5 (CanESM5.0.3). *Geosci. Model Dev.* **12**, 4823–4873 (2019).
72. G. Danabasoglu, J.-F. Lamarque, J. Bacmeister, D. A. Bailey, A. K. DuVivier, J. Edwards, L. K. Emmons, J. Fasullo, R. Garcia, A. Gettelman, C. Hannay, M. M. Holland, W. G. Large, P. H. Lauritzen, D. M. Lawrence, J. T. M. Lenaerts, K. Lindsay, W. H. Lipscomb, M. J. Mills, R. Neale, K. W. Oleson, B. Otto-Bliesner, A. S. Phillips, W. Sacks, S. Tilmes, L. Kampenhout, M. Vertenstein, A. Bertini, J. Dennis, C. Deser, C. Fischer, B. Fox-Kemper, J. E. Kay,

D. Kinnison, P. J. Kushner, V. E. Larson, M. C. Long, S. Mickelson, J. K. Moore, E. Nienhouse, L. Polvani, P. J. Rasch, W. G. Strand, The Community Earth System Model Version 2 (CESM2). *J. Adv. Model. Earth Syst.* **12**, e2019MS001916 (2020).

73. T. van Noije, T. Bergman, P. Le Sager, D. O'Donnell, R. Makkonen, M. Gonçalves-Ageitos, R. Döscher, U. Fladrich, J. von Hardenberg, J.-P. Keskinen, H. Korhonen, A. Laakso, S. Myriokefalitakis, P. Ollinaho, C. Pérez García-Pando, T. Reerink, R. Schrödner, K. Wyser, S. Yang, EC-Earth3-AerChem: A global climate model with interactive aerosols and atmospheric chemistry participating in CMIP6. *Geosci. Model Dev.* **14**, 5637–5668 (2021).
74. O. Boucher, J. Servonnat, A. L. Albright, O. Aumont, Y. Balkanski, V. Bastrikov, S. Bekki, R. Bonnet, S. Bony, L. Bopp, P. Braconnot, P. Brockmann, P. Cadule, A. Caubel, F. Cheruy, F. Codron, A. Cozic, D. Cugnet, F. D'Andrea, P. Davini, C. de Lavergne, S. Denvil, J. Deshayes, M. Devilliers, A. Ducharne, J. Dufresne, E. Dupont, C. Éthé, L. Fairhead, L. Falletti, S. Flavoni, M. Foujols, S. Gardoll, G. Gastineau, J. Ghattas, J. Grandpeix, B. Guenet, L. E. Guez, E. Guilyardi, M. Guimberteau, D. Hauglustaine, F. Hourdin, A. Idelkadi, S. Joussaume, M. Kageyama, M. Khodri, G. Krinner, N. Lebas, G. Levavasseur, C. Lévy, L. Li, F. Lott, T. Lurton, S. Luyssaert, G. Madec, J. Madeleine, F. Maignan, M. Marchand, O. Marti, L. Mellul, Y. Meurdesoif, J. Mignot, I. Musat, C. Ottlé, P. Peylin, Y. Planton, J. Polcher, C. Rio, N. Rochetin, C. Rousset, P. Sepulchre, A. Sima, D. Swingedouw, R. Thiéblemont, A. K. Traore, M. Vancoppenolle, J. Vial, J. Vialard, N. Viovy, N. Vuichard, Presentation and Evaluation of the IPSL-CM6A-LR Climate Model. *J. Adv. Model. Earth Syst.* **12**, e2019MS002010 (2020).
75. S. Yukimoto, H. Kawai, T. Koshiro, N. Oshima, K. Yoshida, S. Urakawa, H. Tsujino, M. Deushi, T. Tanaka, M. Hosaka, S. Yabu, H. Yoshimura, E. Shindo, R. Mizuta, A. Obata, Y. Adachi, M. Ishii, The Meteorological Research Institute Earth System Model Version 2.0, MRI-ESM2.0: Description and basic evaluation of the physical component. *J. Meteorol. Soc. Jpn.* **97**, 931–965 (2019).

Acknowledgments: We thank reviewers for comments and suggestions. We acknowledge the World Climate Research Programme, which, through its Working Group on Coupled Modelling, coordinated and promoted CMIP6. We thank the climate modeling groups for producing and making available their model output, the Earth System Grid Federation (ESGF) for archiving the data and providing access, and the multiple funding agencies who support CMIP6 and ESGF. **Funding:** Y.F. and L.L. were supported by NASA's FINESST under award no. 80NSSC24K1595. P.Z. was supported by the National Science Foundation under grant AGS 2232582. P.Z. and L.L. were supported by NASA grant 80NSSC22K0997. **Author contributions:** Conceptualization: L.L., Y.F., and D.C. Methodology: Y.F., D.C., E.E.C., and L.L. Investigation: Y.F. and L.L. Formal analysis: Y.F. Validation: D.C., E.E.C., P.Z., and L.L. Visualization: Y.F. Resources: L.L. and P.Z. Supervision: L.L. and P.Z. Writing–original draft: Y.F. and L.L. Writing–review and editing: Y.F., D.C., E.E.C., P.F., and L.L. Project administration: L.L. Funding acquisition: P.Z. and L.L. **Competing interests:** The authors declare that they have no competing interests. **Data and materials availability:** All data needed to evaluate the conclusions in the paper are present in the paper and/or the Supplementary Materials. The Met Office HadSST1.1 dataset is available at https://metoffice.gov.uk/hadobs/hadisst/. The Kaplan Extended SST V2 and ERSST V5 datasets are provided by the NOAA/OAR/ESRL PSL, Boulder, Colorado, USA, from their website at https://psl.noaa.gov. The HadSST.4.0.1.0 ensemble is available at https://metoffice.gov.uk/hadobs/hadsst4/data/download.html. The ERSST V5 ensemble is available at https://ncei.noaa.gov/pub/data/cmb/ersst/. All CMIP6 data are available from https://esgf-node.llnl.gov/projects/cmip6/. The NOAA-CIRES 20th Century Reanalysis (V2) data are provided by the NOAA PSL, Boulder, Colorado, USA, from their website at https://psl.noaa.gov.

Submitted 31 July 2024
Accepted 30 April 2025
Published 4 June 2025
10.1126/sciadv.ads1624